Stability Analysis of Sensorless Control of High-Speed Motor in Full-Speed for Aircraft Electric Environment Control

HAO Zhenyang, ZHANG Ya, WANG Yuxuan, CAO Xin, ZHANG Jiawen*

College of Automation Engineering, Nanjing University of Aeronautics and Astronautics, Nanjing 211106, P. R. China

(Received 14 August 2022; revised 28 May 2023; accepted 10 June 2023)

Abstract: This paper takes the high-speed permanent magnet synchronous motor (HSPMSM) control system for electric environment control as the research object. Considering that researches on sensorless control of HSPMSM mainly focuses on algorithm realization and rotor estimation error elimination, we proposes a global stability analysis and parameter design method based on small-signal analysis for sensorless control in full-speed. This method designs the parameters of the position estimation loop based on extended back electromotive force (EMF) method, and studies the influence of the parameters of position estimation loop and speed loop on system stability. Then we uses the root locus to design the upper frequency of I/f control and the lower frequency of extended back EMF method to determine the stable domain of switching. Also, the sensitivity of motor parameters under high temperature are analyzed. Finally, full-speed experiment is carried out on the 45 kW, 40 000 r/min surface mounted HSPMSM for electric environment control. The result shows that the designed loop parameters and switching speed achieve better dynamic and steady-state performance, and the sensitivity of parameter is consistent with the theoretical analysis. It provides a feasible idea for global parameter design and sensitivity analysis of HSPMSM in the full-speed.

Key words: electric environmental control system; high-speed permanent magnet synchronous motor (HSPMSM); sensorless control in full-speed; extended back electromotive force (EMF) method; small signal analysis; parameter robustness

CLC number: V11 **Document code:** A **Article ID:** 1005-1120(2023)04-0434-13

0 Introduction

With the technology progress, the demand for low cost, low carbon emissions, high security and other aspects of the aviation industry is increasing. The aviation system is undergoing a transition from mechanical, hydraulic and pneumatic power systems to electrification[1]. The aircraft's original way of environmental control is to bring hot air from engine through thermodynamic cycle system to obtain a certain pressure and temperature of air to supply the cabin. With the development of aircraft electrification, electric environmental control system has become the direction of concern. The system uses a high-speed motor to drive a compressor with high pressurization ratio to introduce and compress the external air of aircraft, and uses an electric stamping air fan to meet the requirements of pressurization temperature control in cabin. This environmental control method reduces the compensation loss of engine fuel, while the structure of the engine system is simplified and the reliability is improved due to the cancel of air-entraining subsystems or components[2-4]. The B787 environmental control system of Boeing adopts the electric environmental control system, cancels the traditional engine air entraining, and uses the electric compressor to provide the compressed air for the air conditioning system[5].

Considering the high energy density, simple rotor structure and high reliability of high-speed permanent magnet synchronous motor(HSPMSM), it is suitable for electric environment control sys-

*Corresponding author, E-mail address: 1228856835@qq.com.

How to cite this article: HAO Zhenyang, ZHANG Ya, WANG Yuxuan, et al. Stability analysis of sensorless control of high-speed motor in full-speed for aircraft electric environment control[J]. Transactions of Nanjing University of Aeronautics and Astronautics, 2023, 40(4): 434-446.

http://dx.doi.org/10.16356/j.1005-1120.2023.04.005

tem[6-7]. HSPMSM drive control system is one of the key technologies of electric environment control system. In Ref.[8], a method was proposed to obtain the back electromotive force (EMF) of the motor by using direct axis voltage model, the rotor position is tracked by PI controller, and then analyzes the relationship between the bandwidth of estimation loop, speed loop and current loop. Based on Ref.[8], Ref.[9] designed the estimated loop parameters by using damping ratio and natural angular frequency. Ref.[10] used the sensorless control method based on maximum torque-current ratio of hybrid high-frequency injection, combined it with extended back EMF method to achieve sensorless control in whole speed range, and solved the estimation angle error caused by the motor saturation effect. It can be seen that current research on sensorless control system of HSPMSM mainly focuses on algorithm realization, parameter design and rotor estimation error elimination. However, there is no unified design method and good guiding principle for overall stability analysis and parameter sensitivity analysis of sensorless control system of HSPMSM in whole speed range.

Aiming at global parameter design and parameter robustness analysis of HSPMSM with sensorless control, a full-speed stability analysis and design system based on small-signal root locus analysis method is proposed. Firstly, the small-signal model of full speed sensorless control method combined with I/f startup control method and extended back EMF method is established. Secondly, the position estimation loop and outside loop parameters are designed by combining the small-signal analysis method and root locus curve. The speed ranges of stable operation of the I/f method and the extended back EMF method are obtained through stability analysis, and the switching speed is determined based on this. At the same time, the sensitivity analysis of the change of resistance and inductance caused by the high temperature condition and inductance saturation effect is carried out. Finally, the experimental prototype is developed, and the experimental platform of HSPMSM for electric environment control is built. The experiment verifies the effectiveness of parameter design, and the correctness of sensitivity analysis.

1 Sensorless Control in Full-Speed

1.1 Control strategy of I/f constant current variable frequency startup

Since the back EMF in the low-speed section is very small, it is difficult to extract the position information. The method of estimating the rotor position by the back EMF of the motor is almost impossible in the zero-low-speed section[11]. At present, the V/f control method and the I/f control method are commonly used in low-speed section[12-14].

This paper adopts the open-loop start-up control strategy of the I/f constant current variable frequency method. By using a slope function as a given speed, the angle $\Delta\theta^*$ for coordinate transformation is obtained by integrating it. There is a deviation angle $\Delta\theta^*$ between the determined coordinate system by the open loop and the actual rotor coordinate system. According to the motion equation of the motor, the setting range of the starting speed slope $K_{\omega r}$ and its calculation relationship with the torque current i_q^* can be obtained as

$$T_e - T_L = J\frac{d\omega_r}{dt} + B\omega_r \tag{1}$$

$$K_{\omega r} = \frac{d\omega_r}{dt} < \frac{1}{J}\left(\frac{3}{2}p\psi_f i_q^* \cos\Delta\theta - T_L - B\omega_r\right) \tag{2}$$

where T_e is the electromagnetic torque; T_L the load torque; J the rotational inertia; ω_r the angular frequency; B the frictional coefficient; p the number of pole pairs; and ψ_f the permanent flux.

1.2 Sensorless control strategy and smooth switching method based on extended back EMF

Since the load of the high-speed motor for electric environment control is fan load, the load increases with speed, and it is easy to lose stability under I/f control. Therefore, in the middle and high speed section, the speed and position information are usually obtained by calculating the physical quantity containing the speed information of the motor through sampling. The commonly used methods include the flux linkage observation method, the model reference adaptive method and the sliding mode observer method[15-17]. This paper adopts the sensorless control method based on the extended back EMF model of the motor. The estimated value of

extended back EMF is obtained by using the axial voltage equation, and then the rotor position estimation is obtained by adjusting the phase locked loop. The spatial vector diagram of PMSM is shown in Fig.1, where α-β axis is the two-phase stationary coordinate system; d-q axis the two-phase rotating coordinate system; γ-δ axis the two-phase rotating coordinate system estimated by sensorless algorithm; θ the actual rotor angle; $\hat{\theta}$ the estimation of rotor angle; and θ_e the error between actual angle and estimated angle.

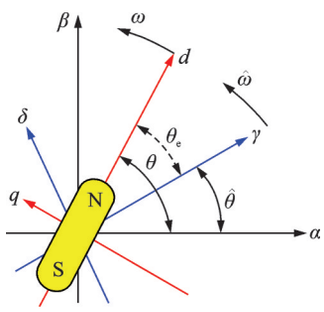

Fig.1 Permanent magnet synchronous motor space vector

According to the voltage equation of PMSM in the d-q rotating coordinate system, the observation value of axial extended back EMF can be obtained, as shown in Eq.(3), in which the current differential term is omitted.

$$\hat{e}_\gamma = \nu_\gamma^* - R_s i_\gamma + \hat{\omega}_r L_q^* i_\delta \tag{3}$$

where $\hat{e}_\gamma$ is the observation value of direct axial extended back EMF; ν_γ^* the direct axis voltage obtained by current loop controller; R_s the stator resistance; i_γ the feedback value of direct axis current; $\hat{\omega}_r$ the estimate angular velocity after filtering; L_q^* the estimated value of direct axis inductance; and i_δ the cross axis inductance feedback value.

Since the γ-axis extended back EMF estimate $\hat{e}_\gamma = E_{ex}^* \sin\theta_e$, when θ_e is approximately 0, $\sin\theta_e \approx \theta_e$, and $\hat{e}_\gamma \approx E_{ex}^* \theta_e$. E_{ex}^* is the estimation of the extended back EMF amplitude. Therefore, the extended back EMF error can be adjusted by PI regulator, and the given value is 0, so the estimated rotor angular velocity is

$$\hat{\omega}_0 = -\left(K_{pe} + \frac{K_{ie}}{s}\right)\hat{e}_\gamma \tag{4}$$

where K_{pe}, K_{ie} are PI regulator parameters and $\hat{\omega}_0$ is the estimate angular velocity before filtering.

The block diagram of speed and rotor position estimation is shown in Fig.2.

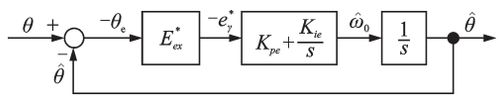

Fig.2 Block diagram of speed estimation

In order to reduce the high frequency ripple, the low-pass filter is introduced to calculate the rotor speed. The cut-off frequency of the low-pass filter is ω_c. The principle block diagram of rotor position estimation based on phase locked loop is shown in Fig.3.

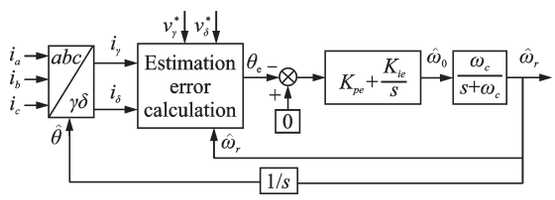

Fig.3 Rotor position estimation based on phase locked loop

Since there is a deviation between the angle of I/f method for coordinate transformation and the estimated angle obtained by the extended back EMF method, direct switching will produce current shock and motor instability. In order to achieve smooth transition, this paper adopts the method of introducing weighted correction factor k_θ, and uses θ^* in open-loop startup process. The transition process transits to the estimation angle $\hat{\theta}$ through the weighted correction factor k_θ. The specific use of coordinate system angle is expressed as

$$\theta = \begin{cases} \theta^* & t < t_{\text{alter1}} \\ (1-k_\theta)\theta^* + k_\theta \cdot \hat{\theta} & t_{\text{alter1}} \leqslant t \leqslant t_{\text{alter2}} \\ \hat{\theta} & t > t_{\text{alter2}} \end{cases} \tag{5}$$

where t_{alter1} is the switch start time and t_{alter2} the switching end time.

When $t = t_{\text{alter1}}$ and $k_\theta = 0$, k_θ increases in switching process. When $t = t_{\text{alter2}}$ and $k_\theta = 1$, the slope of k_θ determines the switching speed. The larger the slope of k_θ, the faster the response speed of current loop and speed loop is required. The experiment is selected according to the expected switching speed.

As shown in Fig.4, the full-speed sensorless control block diagram can be obtained. The I/f control is used at zero low speed. When the switching signal is given, smooth switching control is carried

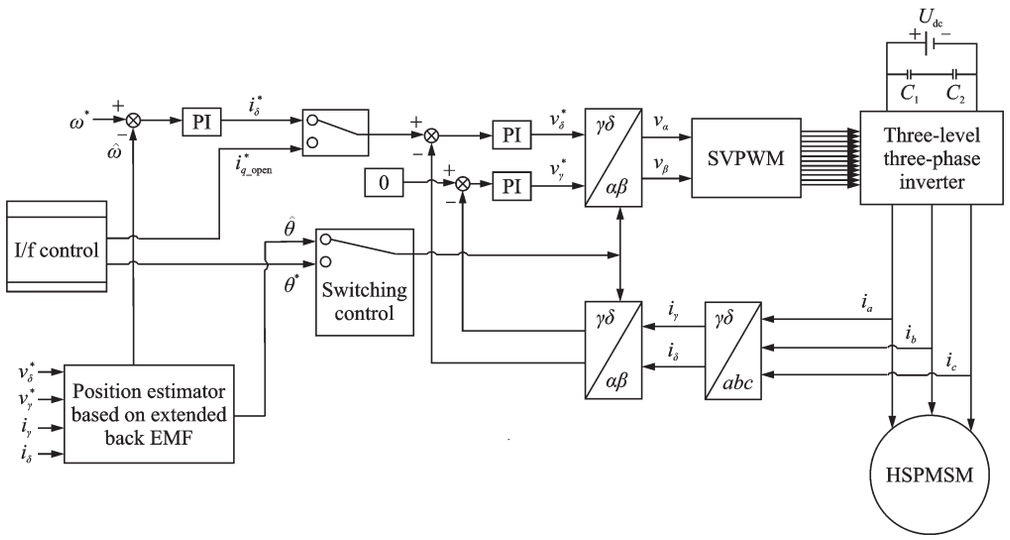

Fig.4 Full-speed position sensorless control block

out. After switching is completed, it runs under sensorless control based on extended back EMF method.

2 Small Signal Stability Analysis

The traditional loop parameters designed through engineering experience are difficult to ensure the stability of the system, and the switching point selected without determining the stability boundary is difficult to ensure successful switching, and the change of resistance and inductance under high temperature and saturation effects affect the stability of the control system. In view of the above problems, this paper proposes a design method of sensorless estimation loop and outer loop parameters, the selection interval of the switching speed and the parameter sensitivity analysis by using the small-signal analysis method.

2.1 Sensorless control strategy and smooth switching method based on extended back EMF

In order to analyze the stability of the system, a small-signal modeling of sensorless control system based on the extended back EMF method is carried out. The voltage and current conversion relationship between the two coordinate axes is

$$\begin{bmatrix} v_d \\ v_q \end{bmatrix} = \begin{bmatrix} \cos\theta_e & -\sin\theta_e \\ \sin\theta_e & \cos\theta_e \end{bmatrix} \begin{bmatrix} v_\gamma^* \\ v_\delta^* \end{bmatrix} \tag{6}$$

$$\begin{bmatrix} i_d \\ i_q \end{bmatrix} = \begin{bmatrix} \cos\theta_e & -\sin\theta_e \\ \sin\theta_e & \cos\theta_e \end{bmatrix} \begin{bmatrix} i_\gamma \\ i_\delta \end{bmatrix} \tag{7}$$

where it is considered that the given PWM inverter is consistent with the output, which is $v_\gamma^* = v_\gamma$, $v_\delta^* = v_\delta$. The state equation of PMSM is established as

$$\begin{cases} pi_d = \dfrac{1}{L_d}\left(v_d - R_s i_d + \omega_r L_q i_q\right) \\ pi_q = \dfrac{1}{L_q}\left(v_q - R_s i_q - \omega_r L_d i_d - \omega_r \psi\right) \\ p\omega_r = \dfrac{P^2}{4J}\left\{\psi i_q + \left(L_d - L_q\right) i_d i_q\right\} - \dfrac{P}{2J} T_L \end{cases} \tag{8}$$

The expression of the speed loop PI controller is

$$pw_1 = \omega_r^* - \hat{\omega}_r, i_q^* = K_{ps}(\omega_r^* - \hat{\omega}_r) + K_{is} w_1 \tag{9}$$

The expression of d-axis current loop PI controller is

$$pw_2 = i_d^* - i_\gamma, v_\gamma^* = K_{pd}\left(i_d^* - i_\gamma\right) + K_{id} w_2 \tag{10}$$

The expression of q-axis current loop PI controller is

$$pw_3 = i_q^* - i_\delta, v_\delta^* = K_{pq}\left(i_q^* - i_\delta\right) + K_{iq} w_3 \tag{11}$$

The expression of estimated loop PI controller is

$$pw_4 = e_\gamma^*, \hat{\omega}_0 = -K_{pe} e_\gamma^* - K_{ie} w_4 \tag{12}$$

where p is the differential operator; w_1, w_2, w_3, w_4 are the intermediate variables; K_{ps}, K_{is}, K_{pd}, K_{id}, K_{pq}, K_{iq} the PI controller parameters of speed loop, d-axis current loop, and q-axis current loop. respectively; ω_r^*, i_d^*, i_q^* the reference values of speed, d-axis current, and q-axis current, respectively; subscripts γ, δ the d, q-axis variables in the estimated

coordinate system.

Low-pass filtering the estimated speed is

$$p\hat{\omega}_r = -\omega_c\hat{\omega}_r + \omega_c\hat{\omega} \tag{13}$$

where ω_c is the cut-off frequency of low-pass filter; and $\hat{\omega}_r$ the estimated rotational speed after low-pass filter.

The expression for sensorless estimation angle error is

$$p\theta_e = \hat{\omega}_r - \omega_r \tag{14}$$

By applying a small disturbance to the system in a steady state, each variable in the system will generate a certain increment near the steady state value, and the state quantity in Eq.(8) can be expressed as a linear increment, the linearized equation of state expression can be obtained as

$$p\Delta\boldsymbol{x}_s = \boldsymbol{A}_s\Delta\boldsymbol{x}_s + \boldsymbol{B}_s\Delta\boldsymbol{u}_s + \boldsymbol{B}_T\Delta T_L \tag{15}$$

where $\boldsymbol{x}_s$ is the system state variable, and $\boldsymbol{u}_s$ the input variable

$$\begin{cases}\Delta\boldsymbol{x}_s = [\Delta i_d \quad \Delta i_q \quad \Delta\omega_r]^T \\ \Delta\boldsymbol{u}_s = [\Delta\nu_d \quad \Delta\nu_q]^T\end{cases} \tag{16}$$

Under small disturbance signal, the angle estimation error is no longer zero, and can be considered as an infinitesimal quantity, so the voltage and current relationship in Eqs.(6,7) are

$$\begin{cases}\Delta\nu_d = \Delta\nu_\gamma^* - \nu_{q0}\Delta\theta_e \\ \Delta\nu_q = \Delta\nu_\delta^* + \nu_{d0}\Delta\theta_e \\ \Delta i_\gamma = \Delta i_d + i_{q0}\Delta\theta_e \\ \Delta i_\delta = \Delta i_q - i_{d0}\Delta\theta_e\end{cases} \tag{17}$$

Substitute Eq.(17) into the controller output state equation and the rotational speed filter equation, namely Eqs.(9—14), the state variable equation of the following form can be obtained, shown as

$$p\Delta\boldsymbol{w} = \boldsymbol{A}_w\Delta\boldsymbol{w} + \boldsymbol{A}_x\Delta\boldsymbol{x}_s + \boldsymbol{B}_r\Delta\boldsymbol{r} \tag{18}$$

$$\begin{cases}\Delta\boldsymbol{w} = [\Delta\hat{\omega}_r \quad \Delta w_1 \quad \Delta w_2 \quad \Delta w_3 \quad \Delta w_4 \quad \Delta\theta_e]^T \\ \Delta\boldsymbol{r} = [\Delta i_d^* \quad \Delta\omega_r^*]^T\end{cases} \tag{19}$$

where Δr is an external given amount.

At the same time, the input quantity $\Delta\boldsymbol{u}_s$ in PMSM is also expressed as a state variable, i.e.

$$\Delta\boldsymbol{u}_s = \boldsymbol{F}_w\Delta\boldsymbol{w} + \boldsymbol{F}_x\Delta\boldsymbol{x}_s + \boldsymbol{F}_r\Delta\boldsymbol{r} \tag{20}$$

Substituting Eq.(20) into the PMSM state equation, the complete system state equation of the control system is obtained as

$$p\begin{bmatrix}\Delta\boldsymbol{x}_s \\ \Delta\boldsymbol{w}\end{bmatrix} = \begin{bmatrix}\boldsymbol{A}_s + \boldsymbol{B}_s\boldsymbol{F}_x & \boldsymbol{B}_s\boldsymbol{F}_w \\ \boldsymbol{A}_x & \boldsymbol{A}_w\end{bmatrix}\begin{bmatrix}\Delta\boldsymbol{x}_s \\ \Delta\boldsymbol{w}\end{bmatrix} + \begin{bmatrix}\boldsymbol{B}_s\boldsymbol{F}_r \\ \boldsymbol{B}_r\end{bmatrix}\Delta\boldsymbol{r} + \begin{bmatrix}\boldsymbol{B}_T \\ 0\end{bmatrix}\Delta T_L \tag{21}$$

According to the linear system theory, in Eq.(21), the matrix $\begin{bmatrix}\boldsymbol{A}_s + \boldsymbol{B}_s\boldsymbol{F}_x & \boldsymbol{B}_s\boldsymbol{F}_w \\ \boldsymbol{A}_x & \boldsymbol{A}_w\end{bmatrix}$ is the state matrix of the system, see the Appendix for specific values.

For a continuous-time linear steady-state control system, the necessary and sufficient condition for asymptotic stability inside the system is that the eigenvalues of the state matrix are all in the left half-plane, and the eigenvalues of the system are obtained as

$$|s\boldsymbol{I} - \boldsymbol{A}(X)| = 0 \tag{22}$$

Since the open-loop I/f control algorithm is current-loop control, the system model is repeated with the above-mentioned parts, and will not be repeated here. The system state matrix is shown in the Appendix.

2.2 Design of rotor position estimator parameters and outer loop parameters

Usually, the parameter design is carried out by bandwidth and phase margin of angle loop. The phase margin and bandwidth of angle estimation loop can be calculated as

$$\begin{cases}\left|G_k(j\omega_g)G_c(j\omega_g)G_p(j\omega_g)\right| = 1 \\ \phi_m = \arg\left[G_k(j\omega_g)G_c(j\omega_g)G_p(j\omega_g)\right] + \pi\end{cases} \tag{23}$$

where ω_g is the angle loop bandwidth; and ϕ_m the phase margin. The expressions of bandwidth and phase margin can be obtained by solving Eq.(23), i.e.

$$\begin{cases}\omega_g = \sqrt{\dfrac{K_1^2 + \sqrt{K_1^4 + 4K_2^2}}{2}} \\ \phi_m = \arctan\dfrac{K_{pe}}{K_{ie}}\sqrt{\dfrac{K_1^2 + \sqrt{K_1^4 + 4K_2^2}}{2}}\end{cases} \tag{24}$$

where $K_1 = E_{ex}^*K_{pe}$, $K_2 = E_{ex}^*K_{ie}$.

Express K_{pe} and K_{ie} in terms of bandwidth and phase margin as

$$\begin{cases} K_{pe}=\dfrac{\omega_g}{E_{ex}^*}\sqrt{\dfrac{\left(\tan\phi_m\right)^2}{1+\left(\tan\phi_m\right)^2}} \\ K_{ie}=\dfrac{\omega_g^2}{E_{ex}^*}\sqrt{\dfrac{1}{1+\left(\tan\phi_m\right)^2}} \end{cases} \tag{25}$$

In engineering, in order to abtain a good transition process of estimated loop, the phase angle margin is generally 30°—60°. In order to prevent crosstalk with current loop, the bandwidth of estimated loop is generally much smaller than that of current loop, and it is expected that its bandwidth is slightly larger than that of speed loop to ensure that estimated loop has a faster response than speed loop[18], so the range of bandwidth of estimated loop is usually choosed as

$$\omega_{sc}<\omega_g\ll\omega_{cc} \tag{26}$$

where ω_{sc} is the speed loop bandwidth, and ω_{cc} the current loop bandwidth. Using the above method to design each loop can only roughly estimate the parameters and debug it in the way of engineering experience, the actual system stability cannot be guaranteed. Therefore, according to the small signal model in Section 2.1, this paper analyzes the stability of the system under different estimated loop parameters.

The speed loop bandwidth is set to 10 Hz, the estimated loop bandwidth is 0—100 Hz, and the system root locus of the current loop bandwidth changing in the range of 200—1 600 Hz is shown in Fig.5.

When the current loop bandwidth is small, the root locus of the system is very close to imaginary axis, and the stability is poor. When the current loop bandwidth is less than 600 Hz, the root locus of higher part of estimated loop bandwidth is located on the right side of imaginary axis. With the increase of current loop bandwidth, the root locus of the system gradually moves away from imaginary axis, and the stability is improved. However, when current loop bandwidth is greater than 1 000 Hz, the improvement of the system stability is no longer obvious. It is not meaningful to continue to increase current loop bandwidth. Therefore, the current loop bandwidth is selected as 1 000 Hz.

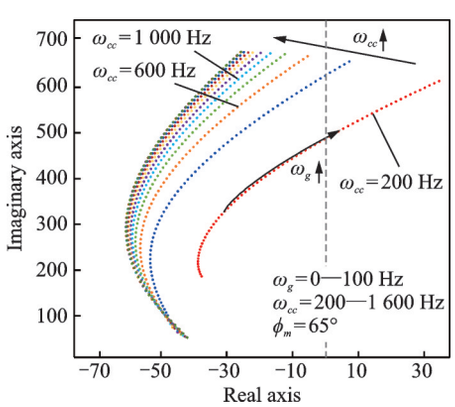

Fig.5 Root locus when estimate loop and current loop parameters change

Set the current loop closed-loop bandwidth value to 1 000 Hz, the speed loop closed-loop bandwidth to 10 Hz, the speed estimation low-pass filter to 300 Hz, and the estimated loop phase angle margin to 65°. The characteristic root locus of the system when the estimated loop bandwidth is from 0 to 100 Hz is drawn, and the dominant root locus near imaginary axis is selected for analysis, as shown in Fig.6.

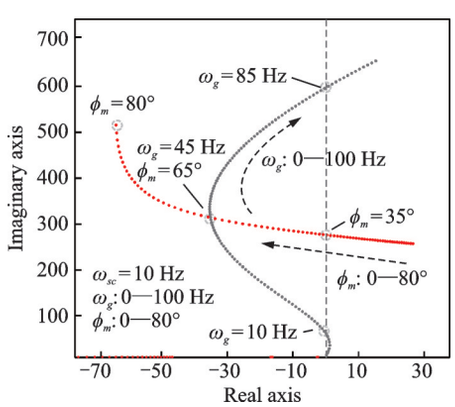

Fig.6 Root locus when estimate loop parameters

When the estimated loop bandwidth is low, the root locus of the system is on the right side of imaginary axis, and then gradually moves away from imaginary axis to upper left, and then gradually approaches imaginary axis and moves upward to right after passing an inflection point. It can be seen that the system is unstable when the bandwidth of estimation loop is lower than the bandwidth of speed loop; when the bandwidth of estimation loop is increased, the response speed of the system is accelerated and the stability is improved; when the band-

width continues to increase, although the response speed of the system increases, the system will oscillate.

Set the angle estimation loop bandwidth at 45 Hz, and the root locus is drawn with a phase margin of 0—80°. As the phase margin increases, the root locus of the system moves to left, and the damping ratio of estimated loop around 65° is calculated to be 0.707. By estimating the root locus when loop parameters change, appropriate loop parameters can be selected according to actual system's index requirements for estimation loop.

The above analysis is only for case where the bandwidth of speed loop is 10 Hz. In actual system, speed loop also affects system stability. The calculation formula of speed loop[19] is

$$K_{ps}=\frac{J\omega_{sc}}{K_t},\qquad K_{is}=\frac{B\omega_{sc}}{K_t} \tag{27}$$

where J is the motor torque; K_t the torque coefficient of the motor, and its calculation formula is

$$K_t=1.5p_n\psi_f \tag{28}$$

where ψ_f is the permanent magnet flux linkage; and p_n the number of motor pole pairs.

It can be seen from Fig. 7 that when the bandwidth of speed loop changes from 5 Hz to 45 Hz, the root locus moves to imaginary axis, and the critical point of system stability is 36 Hz. Although the increase of speed loop bandwidth can increase the response speed of speed loop, the system stability is also reduced accordingly.

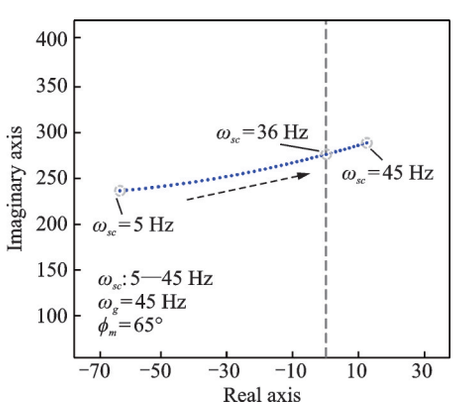

Fig.7 Root locus when speed loop parameters change

Fig.8 shows the root locus of estimated loop bandwidth varying from 0 to 100 Hz when the speed loop bandwidths are 5, 10, and 15 Hz.

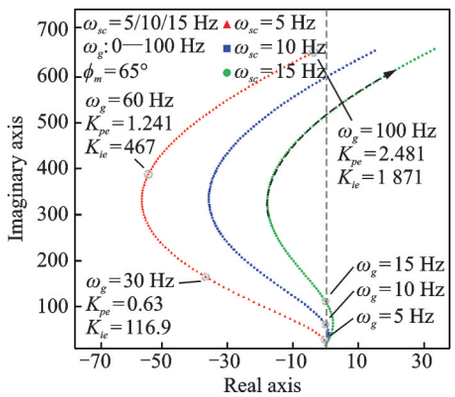

Fig.8 Root locus when parameters of estimation loop and speed loop change

When the bandwidth of speed loop increases from 5 Hz to 15 Hz, the system stability decreases, and the eigenvalue of lower part of angle loop bandwidth in right half plane of imaginary axis also increases, that is, the system is unstable when the bandwidth of angle loop is smaller than the bandwidth of speed loop. The lower the speed loop bandwidth is, the system stability is improved and the estimated loop parameters are selected to have a larger stable range, but the speed response is slower.

2.3 Selection of stable switching interval

As I/f control given current is constant, and the compressor load increases with the increase of speed, the higher the speed, the easier it is to lose step. Therefore, the selection of a suitable switching point between two algorithms is necessary to ensure the success of switching. This section uses small-signal model of the system to select the switching interval through stability analysis.

Fig. 9 shows the overall root locus of the system and the upper half of the two root locus close to

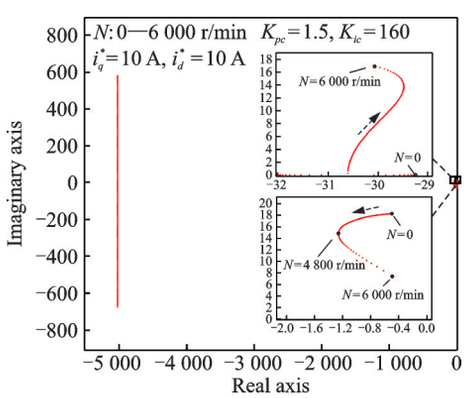

Fig.9 Root locus when I/f control rotational speed changes

imaginary axis when the rotational speed of I/f method changes. Only the two root locus close to imaginary axis are analyzed. Since one of them always has a negative real part, therefore, only the stability analysis of the root locus close to imaginary axis is analysed.

The speed of rotor is changed from 0 to 6 000 r/min, and the step of speed is set as 100 r/min. At 4 800 r/min, the root locus is closest to imaginary axis, and the critical stability range is about 6 000 r/min. At low speed, the root locus is very close to imaginary axis, and the system will oscillate. Similarly, the root locus of extended back EMF method when the rotational speed changes at a low speed is analyzed, and the results are shown in Fig.10.

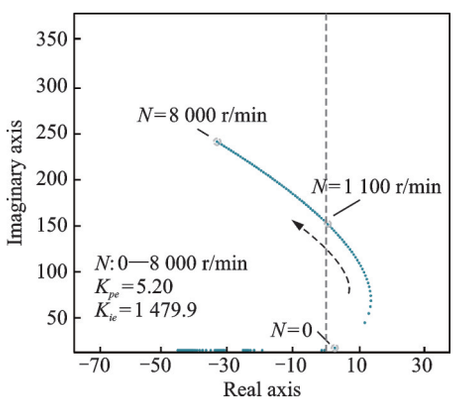

Fig.10 Root locus of extended back-EMF method at low speed when rotational speed changes

At zero and low speed, the root locus of the system is on the right side of imaginary axis, and the critical stability value is about 1 100 r/min. As the speed continues to increase, the system stability increases. The two algorithms are stable within the range of 1 100 r/min to 6 000 r/min, and the selection of switching point should also be within this range to ensure the success of switching and the stability of full-speed domain control.

2.4 Sensitivity and stability analysis of motor parameters

The extended back EMF calculation formula in algorithm includes stator resistance and q-axis inductance parameters. Due to the saturation effect of the inductance and the motor stator resistance will increase under high temperature operation, the motor parameters will be inaccurate. When the deviation between actual resistance of the motor and the resistance set in algorithm is ΔR_s, the observed value of d-axis extended back EMF is

$$\hat{e}_{\gamma\_\Delta R_s} = (E_{ex} + \Delta R_s i_\gamma)\sin\theta_e \tag{29}$$

When there is a deviation between motor resistance parameter setting and actual resistance, the phase calculated by the back EMF has no deviation, only the amplitude is different. When the deviation between actual inductance of the motor and the inductance set in algorithm is ΔL_q, the observed value of d-axis extended back EMF is

$$\hat{e}_{\gamma\_\Delta L_q} = \sqrt{E_{ex}^2 + (\omega \Delta L_q i_\delta)^2}\sin(\theta_e - \Delta\theta) \tag{30}$$

where $\Delta L_q = L_q^* - L_q$, $\Delta\theta = \arctan\left(\dfrac{\Delta L_q i_\delta}{\psi_f}\right)$.

When the inductance deviation is set as ΔL_q in algorithm, the calculated value of extended back EMF produces the observed phase lag, that is, the angle estimation error of $\Delta\theta$ occurs. The lag angle is related to ΔL_q, δ-axis current and flux linkage, and the angle error is more obvious due to the exponential relationship between compressor load and rotational speed[20]. The root locus of inductance changes under rated conditions is analyzed.

It can be seen from Fig.11 that the real part of the system root locus increases with the increase of the ratio of reference inductance to actual inductance, and enters unstable region after exceeding the critical value of 1.41, and the sensitivity becomes greater. If the ratio is less than 1, the system stability is slightly improved and the sensitivity becomes low.

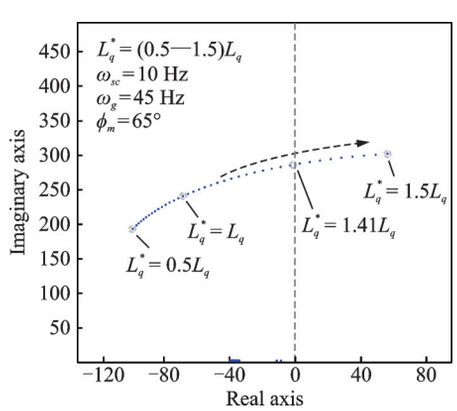

Fig.11 Root locus when inductance changes

3 Experimental Verification

3.1 Introduction to experimental platform

The overall hardware platform of the system includes main control board, drive board, main power circuit, upper computer, motor and load. The main control board is composed of DSPTMS320F28335 and FPGA (EP2C8Q208I8N) as the core. The main power topology is a three-level inverter, each phase is composed of two three-level IGBT bridge arm modules in parallel, and the DC side is composed of upper and lower split capacitors in series. The experimental platform of HSPMSM control system for electric environmental control is shown in Fig.12. The HSPMSM for electric environmental control is fed into oil pump through an air compressor to cool and lubricate the bearing. The motor is of air-cooled structure. PT100 thermistor is embedded in winding, air inlet and outlet bearings. The motor temperature can be monitored through temperature transmitter.

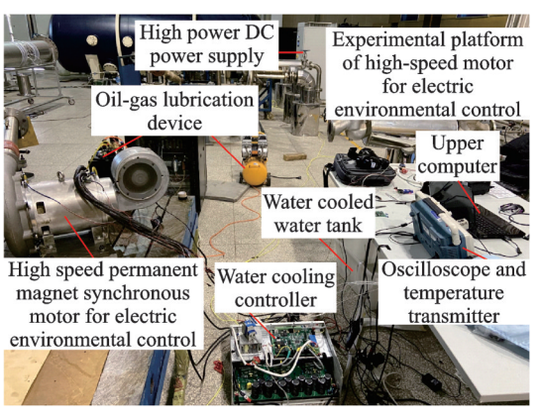

Fig.12 High-speed motor control system experimental platform for electric environment control

3.2 Experimental verification of low-speed startup and switching strategy

Firstly, the I/f startup and switching control strategy is verified by experiments. Surface mounted PMSM is selected, and the parameters are listed in Table 1. In Table 1, rated current refers to the amplitude of phase current. The reasonable switching speed and estimated loop bandwidth obtained in Section 2 are 2 000 r/min and 45 Hz, respectively. The I/f start-up slope is set to 2 000 (r/min) /s, the target start-up speed is 2 000 r/min, when it reaches 2 000 r/min, the transition switch is triggered, and the target speed in switching process is set to 5 000 r/min. According to torque current calculation formula in Section 1.1, the minimum starting current is 10.22 A. In order to leave a certain margin, the current i_q^* is set as 15 A.

Table 1 Parameters of prototype

Parameter	Value
Number of stator pole	1
Rated power / kW	45
Rated current / A	155
Rated voltage of motor / V	540
Rated speed / ($r \cdot min^{-1}$)	40 000
Rated torque / ($N \cdot m^{-1}$)	10.42
Phase resistance /Ω	0.005 3
Phase inductance /μH	181.47
Rotor flux linkage / Wb	0.045 6
Moment of inertia / ($kg \cdot m^3$)	3e−4
Switching frequency / Hz	16 000

It can be seen from Fig.13 that the target speed reaches 2 000 r/min after about 1 s of open-loop startup. As the speed loop is introduced in switching phase, the motor current gradually decreases until the coordinate system completely transitions to the position estimation coordinate system. The waveforms before and after switching are shown in Fig.14.

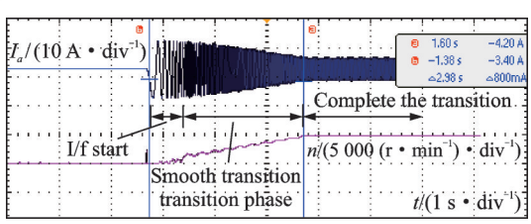

Fig.13 Smooth transition switching process current and speed waveform

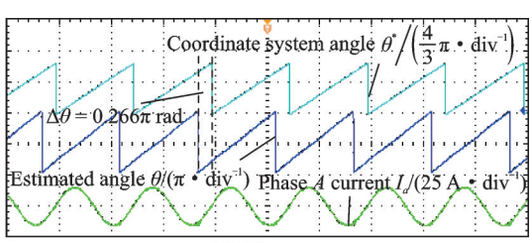

(a) I/f startup

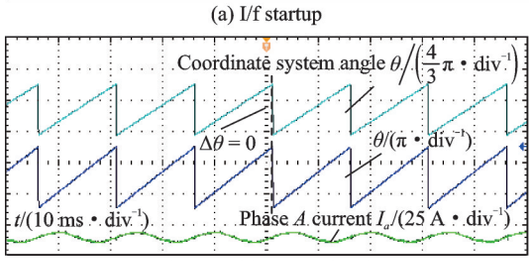

(b) Transition completed

Fig.14 Transition process angle waveform

3.3 Loop parameter design and motor parameter sensitivity test verification

The bandwidth of different angle estimation loop and speed loop is verified by experiments.

As shown in Fig.15, when the bandwidth of angle estimation loop is 30 Hz, the maximum angle error reaches 0.104 rad during speed increase process, and the speed overshoot is serious. The maximum current is about 50 A. The system is stable but there is a large estimation error. According to the root locus analysis results in Section 2, when the bandwidth of angle estimation loop is 45 Hz, the maximum angle error is about 0.025 rad, the maximum current is 35 A, the steady-state error of angle estimation is almost zero, and the steady-state speed fluctuation is small. It can be judged that the decrease of estimated loop bandwidth can reduce the steady-state estimated speed ripple, but the estimation error in the speed increase process is increased.

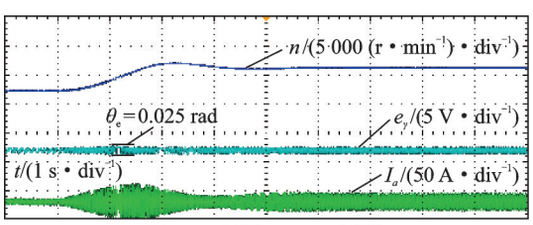

(a) $\omega_{sc}=10$ Hz, $\omega_g=45$ Hz

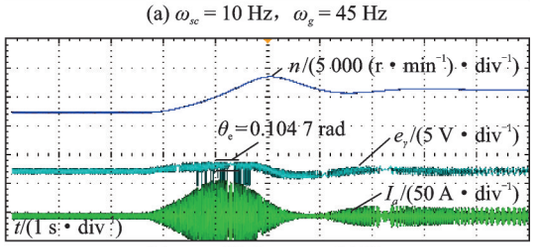

(b) $\omega_{sc}=10$ Hz, $\omega_g=30$ Hz

Fig.15 Speed-up response under different loop bandwidths

Although increasing estimated loop bandwidth can improve its dynamic performance, the root locus analysis shows that the continuous increase of estimated loop bandwidth will lead to system instability. Fig.16(a) shows the experimental waveform of 60 Hz estimated loop bandwidth. The estimation error during speed increase is almost zero, but the high-frequency ripple of speed estimation is more obvious. In addition, under 60 Hz estimated loop bandwidth, change the speed loop bandwidth to 20 Hz, as shown in Fig.16(b), the speed response oscillation intensifies.

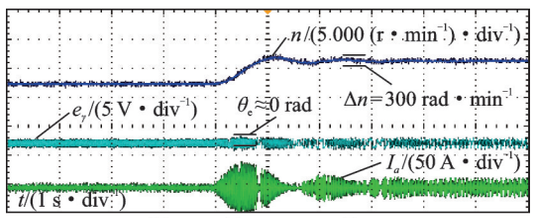

(a) $\omega_{sc}=10$ Hz, $\omega_g=60$ Hz

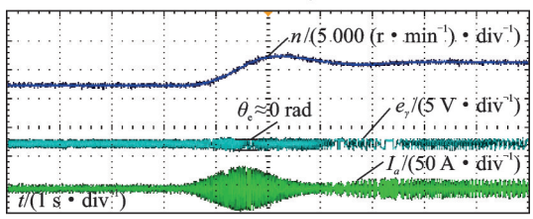

(b) $\omega_{sc}=20$ Hz, $\omega_g=60$ Hz

Fig.16 Speed response at different loop bandwidths

Since the motor parameters only change when the temperature is high and the inductance is saturated, the parameter error is simulated by changing the reference inductances l_q^* and r_s^* in the control algorithm, and the influence of parameter inductance on the control system is judged by the phase current and whether the speed is stable. The results are shown in Fig.17.

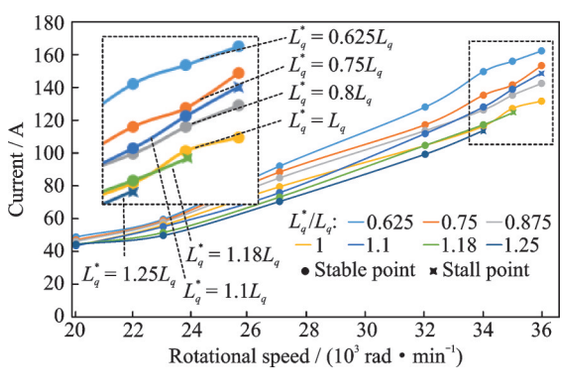

Fig.17 Magnitude of current when inductance changes in control algorithm

When the ratio of reference inductance to actual inductance is 0.625, current increases at fixed speed due to the increase of angle error, and the system is still stable. When the ratio of reference inductance to actual inductance is 1.25, it diverges at about 34 000 r/min, and there is a small deviation between the result and the unstable point of theoretical analysis. It is speculated that it is caused by inductance change or measurement error in actual working conditions. When the stator resistance changes, the control algorithm is hardly affected.

3.4 Verification of sensorless control and function of electric environmental control system in medium and high speed section

In order to verify the stability of sensorless control algorithm in high-speed, the steady-state speed experiment of 40 000 r/min is carried out.

Fig.18 shows the estimated angle and phase current waveform at the speed of 40 000 r/min, the system can run stably, and the sinusoidal degree of current waveform is good. The phase current amplitude is 155 A, the DC side input power is 45 kW, and the current frequency is 666.67 Hz.

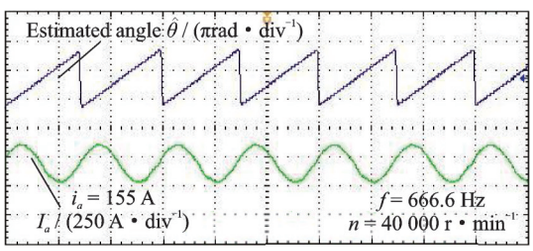

Fig.18 Steady state current and angle waveform at 40 000 r/min

4 Conclusions

Based on the 40 000 r/min, 45 kW HSPMSM for electric environment control experimental platform, this paper analyzes full speed domain stability of the sensorless control method combined with the I/f startup method and the extended back EMF method and carries out relevant experiments. Finally, the following conclusions are drawn:

(1) A global stability design and analysis method for full speed domain sensorless control system of high-speed motor is proposed. Using the small signal analysis method, the parameters of estimation loop and outer loops under extended back EMF method are designed, and the overall trend of the system stability with loop parameters is obtained. The specific parameters are further determined based on dynamic index.

(2) Using stability analysis, the maximum stable operation frequency of I/f method and the minimum stable operation frequency of extended back EMF method are determined, and the switching stability region of sensorless control is obtained. Based on this, the switching range of the system is 1 100—6 000 r/min, realizing the stable operation in full speed region.

(3) The influence of motor parameters on the stability and sensitivity of the system is analyzed. It is concluded that under the extended back EMF method, when L_q^*/L_q=0.5—1, the sensitivity of the system is low and the influence on robustness of the system is not obvious; When L_q^*/L_q=1—1.5, the sensitivity of the system increases significantly. The critical stable value of the system inductance is L_q^*/L_q=1.41. The influence of resistance variation on system stability can be almost ignored.

Appendix

$$\boldsymbol{A}_s=\begin{bmatrix} -\dfrac{R_s}{L_d} & \dfrac{L_q\omega_{r0}}{L_d} & \dfrac{L_q i_{q0}}{L_d} \\ -\dfrac{L_d\omega_{r0}}{L_q} & -\dfrac{R_s}{L_q} & -\dfrac{L_d i_{d0}+\psi}{L_q} \\ \dfrac{P^2(L_d-L_q)i_{q0}}{4J} & \dfrac{P^2\{\psi+(L_d-L_q)i_{d0}\}}{4J} & 0 \end{bmatrix}$$

$$\boldsymbol{B}_s=\begin{bmatrix} \dfrac{1}{L_d} & 0 \\ 0 & \dfrac{1}{L_q} \\ 0 & 0 \end{bmatrix},\quad \boldsymbol{B}_T=\begin{bmatrix} 0 \\ 0 \\ -\dfrac{P}{2J} \end{bmatrix}$$

$$\boldsymbol{A}_w=\begin{bmatrix} -\omega_c-K_{pe}L_q^*i_{\partial 0}\omega_c & 0 & -\omega_c K_{pe}K_{id} & 0 & -\omega_c K_{ie} & \omega_c K_{pe}K_{pd}i_{q0}+K_{pe}L_q^*\hat{\omega}_{r0}i_{d0}\omega_c \\ -1 & 0 & 0 & 0 & 0 & 0 \\ 0 & 0 & 0 & 0 & 0 & -i_{q0} \\ -K_{ps} & K_{is} & 0 & 0 & 0 & i_{d0} \\ 0 & 0 & K_{id} & 0 & 0 & -K_{pd}i_{q0} \\ 1 & 0 & 0 & 0 & 0 & 0 \end{bmatrix}$$

$$\boldsymbol{A}_x=\begin{bmatrix} \omega_c K_{pe}K_{pd} & -K_{pe}L_q^*\hat{\omega}_{r0}\omega_c & 0 \\ 0 & 0 & 0 \\ -1 & 0 & 0 \\ 0 & -1 & 0 \\ -K_{pd} & 0 & 0 \\ 0 & 0 & -1 \end{bmatrix},\boldsymbol{B}_r=\begin{bmatrix} -\omega_c K_{pe}K_{pd}+K_{pe}R_s^*\omega_c & 0 \\ 0 & 1 \\ 1 & 0 \\ 0 & K_{ps} \\ K_{pd} & 0 \\ 0 & 0 \end{bmatrix}$$

$$F_w=\begin{bmatrix}0 & 0 & K_{id} & 0 & 0 & -i_{q0}K_{pd}\\ -K_{pq}K_{ps} & K_{pq}K_{is} & 0 & K_{iq} & 0 & K_{pq}i_{d0}+\nu_{\gamma 0}^*\end{bmatrix}$$

$$F_x=\begin{bmatrix}-K_{pd} & 0 & 0\\ 0 & -K_{pq} & 0\end{bmatrix},\quad F_r=\begin{bmatrix}K_{pd} & 0\\ 0 & K_{pq}K_{ps}\end{bmatrix}$$

State equation of small signal modeling system based on I/f control method

$$p\boldsymbol{x}=f(\boldsymbol{x},\boldsymbol{u})$$

$$\boldsymbol{x}=\begin{bmatrix}i_d^* & i_q^* & \omega_r & \delta & w_1 & w_2\end{bmatrix}^{\mathrm{T}}$$

$$\boldsymbol{u}=\begin{bmatrix}i_{\mathrm{dref}}^* & i_{\mathrm{dref}}^* & \omega_e\end{bmatrix}^{\mathrm{T}}$$

The form of linearized system matrix is: $p\Delta\boldsymbol{x}=\boldsymbol{A}_1\Delta\boldsymbol{x}+\boldsymbol{B}_1\Delta\boldsymbol{u}$, where the state transition matrix is

$$\boldsymbol{A}_1=\begin{bmatrix}-\frac{R_s}{L}-\frac{K_{pc}}{L} & \omega_{e0} & \frac{\cos(\delta_0)\psi}{L} & -\frac{\omega_{r0}\sin(\delta_0)\psi}{L} & \frac{K_{ic}}{L} & 0\\ -\omega_{e0} & -\frac{R_s}{L}-\frac{K_{pc}}{L} & -\frac{\sin(\delta_0)\psi}{L} & -\frac{\omega_{r0}\cos(\delta_0)\psi}{L} & 0 & \frac{K_{ic}}{L}\\ \frac{3\cos(\delta_0)\psi P^2}{2J} & \frac{3\sin(\delta_0)\psi P^2}{2J} & 0 & \frac{3\sin(\delta_0)i_{q0*}\psi P^2}{2J} & 0 & 0\\ 0 & 0 & -1 & 0 & 0 & 0\\ -1 & 0 & 0 & 0 & 0 & 0\\ 0 & -1 & 0 & 0 & 0 & 0\end{bmatrix}$$

References

[1] CAO W, MECROW B C, ATKINSON G J, et al. Overview of electric motor technologies used for more electric aircraft (MEA)[J]. IEEE transactions on industrial electronics, 2012, 59(9): 3523-3531.

[2] ZHANG Zhuoran, YU Li, LI Jincai, et al. Advanced aviation electrical systems in the context of aircraft electrification [J]. Journal of Nanjing University of Aeronautics and Astronautics, 2017, 49(5): 622-634. (in Chinese)

[3] XU Liyun. Research on environmental control system of civil aircraft[J]. Aeronautical Science and Technology, 2015, 26(7): 42-45. (in Chinese)

[4] HUANG Hui, CUI Dandan, CUI Gaowei. Comparative analysis of performance of bleed air environmental control system and all-electric environmental control system [J]. China Science and Technology Information, 2013(15): 132-135. (in Chinese)

[5] MENG Fanxin, WANG Ruiqi, GAO Zanjun, et al. Research on key technologies of electric environment control system for multi-electric aircraft[J]. Aeronautical Science and Technology, 2018, 29(2): 1-8. (in Chinese)

[6] JIANG Liangliang. The trade-off analysis method of civil aircraft air source system architecture[J]. Science & Technology Vision, 2017(8): 31. (in Chinese)

[7] TEGOPOULOS J A. Electrical machines for electromotion and their design[C]//Proceedings of the 21st IEEE Convention of the Electrical and ELectronic Engineers in Israel, 2000. Tel-Aviv, Israel: IEEE, 2000. (in Chinese)

[8] CHENG Boshi. Electric drag automatic control system [M]. Beijing: China Mechine Press, 2010.

[9] SEOK J, LEE J, LEE D. Sensorless speed control of nonsalient permanent-magnet synchronous motor using rotor-position-tracking PI controller [J]. IEEE transactions on industrial electronics, 2006, 53(2): 399-405.

[10] TSUJI M, KOJIMA K, MANGINDAAN G M C, et al. Stability study of a permanent magnet synchronous motor sensorless vector control system based on extended EMF model[J]. IEEE Journal of Industry Applications, 2012, 1(3): 148-154.

[11] LIN C, NI Q, ZHAN H, et al. Maximum torque per ampere sensorless control of synRM based on mixed signal injection and extended back-EMF [C]// Proceedings of the 2021 24th International Conference on Electrical Machines and Systems (ICEMS). [S.l.]: [s.n.], 2021: 1720-1724.

[12] ZHANG Z. Sensorless control of synchronous machines using fundamental back-EMF voltage—A review [J]. IEEE Transactions on Power Electronics, 2022. DOI: 10.1109/TPEL.2022.3162963.

[13] JO G J, CHOI J W. Rotor field-oriented V/f drive system implementation with oscillation suppression compensator in induction motors [J]. IEEE Journal of Emerging and Selected Topics in Power Electronics, 2021, 9(3): 2745-2758.

[14] CHEN D Z, LU K Y, WANG D, et al. A small-signal stability study for open-loop I-f control of permanent magnet synchronous machine drives [C]// Proceedings of the 2021 4th International Conference on Energy, Electrical and Power Engineering (CEEPE). [S.l.]: IEEE, 2021: 405-409.

[15] WANG C, GOU L, DONG S, et al. Sensorless control of IPMSM based on super-twisting sliding mode observer with CVGI considering flying start[J]. IEEE Transactions on Transportation Electrification, 2022, 8(2): 2106-2117.

[16] ZHENG Shida. Research on speed pulsation suppres-

sion method of position sensorless permanent magnet synchronous compressor for air conditioner[D]. Hangzhou: Zhejiang University, 2020. (in Chinese)

[17] VEMAGIRI T, SAVARAPU S. Fuzzy logic based sensorless control of five phase IPMSM drives through HF-SVI into third harmonic space[C]//Proceedings of the 2021 IEEE 2nd International Conference on Applied Electromagnetics, Signal Processing, & Communication (AESPC). [S.l.]: IEEE, 2021: 1-6.

[18] GOU Lifeng. Research on key technology of traction motor without position/speed sensor for rail transit vehicle[D]. Beijing: Beijing Jiaotong University, 2021. (in Chinese)

[19] WANG Lina, ZHU Hongyue, YANG Zongjun. Parameter setting method of PI controller for permanent magnet synchronous motor speed control system[J]. Transactions of China Electrotechnical Society, 2014, 29(5): 104-117. (in Chinese)

[20] ZHAO Bo. Experimental and numerical study of in-ternal flow in a high-speed centrifugal compressor with a vane diffuser[D]. Shanghai: Shanghai Jiao Tong University, 2020. (in Chinese)

Acknowledgements This work was supported in part by the National Natural Science Foundation of China (No. 52077100), and the Aeronautical Science Foundation of China (No.201958052001).

Authors Prof. **HAO Zhenyang** received the bachelor's degree in electrical engineering from Nanjing Normal University, in 2004, and the M.S. and Ph.D. degrees in power electronics and motion drive from the Nanjing University of Aeronautics and Astronautics, in 2007 and 2010. He has been an professor in the Department of Electrical Engineering, Nanjing University of Aeronautics and Astronautics, since 2022. His research interests include sensorless control technology, new energy power electronic conversion technology, aviation power supply and power actuator technology, electric vehicle motor design, and driving technology.

Ms. **ZHANG Ya** received the B.S. degree in electrical engineering and automation from the Nanjing University of Aeronautics and Astronautics, China, in 2021, where she is currently pursuing the M. S. degree in electrical engineering. Her research interest includes sensorless control technology.

Author contributions Prof. **HAO Zhenyang** designed the study, complied the models, conducted the analysis, interpreted the results and wrote the manuscript. Ms. **ZHANG Ya** contributed to data and model components for the PMSM sensorless model. Mr. **WANG Yuxuan** contributed to data for the stability analysis. Prof. **CAO Xin** contributed to the hardware platform of the system. Mr. **ZHANG Jiawen** contributed to the discussion and background of the study. All authors commented on the manuscript draft and approved the submission.

Competing interests The authors declare no competing interest.

(Production Editor: SUN Jing)

飞机电动环控用高速电机全速域无位置控制稳定性分析

郝振洋，张　雅，汪禹萱，曹　鑫，张嘉文

（南京航空航天大学自动化学院，南京 211106，中国）

摘要：以飞机电动环控用高速永磁同步电机(High-speed permanent magnet synchronous motor，HSPMSM)控制系统为研究对象，考虑到HSPMSM无传感器控制的研究主要集中在算法实现和转子估计误差消除方面，本文提出了一种基于小信号分析的无传感器全速控制全局稳定性分析和参数设计方法。该方法在扩展反电动势法的基础上设计了位置估计环的参数，并建立了位置估计环和速度环的参数对系统稳定性的影响。其次，本文使用根轨迹来设计I/f控制能够运行的最高转速和扩展反电动势法能够运行的最低转速，以确定算法切换的稳定转速。同时分析了电机参数在高温下的灵敏度。最后，在45 kW、4 000 r/min表贴式HSPMSM上进行了全速域电动环控实验。结果表明，本文设计的回路参数和切换转速具有更好的动态和稳态性能，参数的灵敏度与理论分析一致，为HSPMSM的全局参数设计和灵敏度分析提供了可行的思路。

关键词：电动环控系统；高速永磁同步电机；全速域无位置传感器控制；扩展反电势法；小信号分析；参数鲁棒性